



<b>Publication Year</b>	2019
<b>Acceptance in OA @INAF</b>	2020-12-15T11:58:42Z
<b>Title</b>	Growth Model Interpretation of Planet Size Distribution
<b>Authors</b>	Li Zeng; Stein B. Jacobsen; Dimitar D. Sasselov; Michail I. Petaev; Andrew Vanderburg; et al.
<b>DOI</b>	10.1073/pnas.1812905116
<b>Handle</b>	<a href="http://hdl.handle.net/20.500.12386/28855">http://hdl.handle.net/20.500.12386/28855</a>
<b>Journal</b>	PROCEEDINGS OF THE NATIONAL ACADEMY OF SCIENCES OF THE UNITED STATES OF AMERICA
<b>Number</b>	116



# Growth model interpretation of planet size distribution

Li Zeng<sup>a,b,1</sup>, Stein B. Jacobsen<sup>a</sup>, Dimitar D. Sasselov<sup>b</sup>, Michail I. Petaev<sup>a,b</sup>, Andrew Vanderburg<sup>c</sup>, Mercedes Lopez-Morales<sup>b</sup>, Juan Perez-Mercader<sup>a</sup>, Thomas R. Mattsson<sup>d</sup>, Gongjie Li<sup>e</sup>, Matthew Z. Heising<sup>b</sup>, Aldo S. Bonomo<sup>f</sup>, Mario Damasso<sup>f</sup>, Travis A. Berger<sup>g</sup>, Hao Cao<sup>a</sup>, Amit Levi<sup>b</sup>, and Robin D. Wordsworth<sup>a</sup>

<sup>a</sup>Department of Earth and Planetary Sciences, Harvard University, Cambridge, MA 02138; <sup>b</sup>Center for Astrophysics | Harvard & Smithsonian, Department of Astronomy, Harvard University, MA 02138; <sup>c</sup>Department of Astronomy, The University of Texas at Austin, Austin, TX 78712; <sup>d</sup>High Energy Density Physics Theory Department, Sandia National Laboratories, Albuquerque, NM 87185; <sup>e</sup>School of Physics, Georgia Institute of Technology, Atlanta, GA 30313; <sup>f</sup>Istituto Nazionale di Astrofisica—Osservatorio Astrofisico di Torino, 10025 Pino Torinese, Italy; and <sup>g</sup>Institute for Astronomy, University of Hawaii, Honolulu, HI 96822

Edited by Neta A. Bahcall, Princeton University, Princeton, NJ, and approved March 21, 2019 (received for review July 26, 2018)

The radii and orbital periods of 4,000+ confirmed/candidate exoplanets have been precisely measured by the *Kepler* mission. The radii show a bimodal distribution, with two peaks corresponding to smaller planets (likely rocky) and larger intermediate-size planets, respectively. While only the masses of the planets orbiting the brightest stars can be determined by ground-based spectroscopic observations, these observations allow calculation of their average densities placing constraints on the bulk compositions and internal structures. However, an important question about the composition of planets ranging from 2 to 4 Earth radii ( $R_{\oplus}$ ) still remains. They may either have a rocky core enveloped in a  $H_2$ –He gaseous envelope (gas dwarfs) or contain a significant amount of multicomponent,  $H_2O$ -dominated ices/fluids (water worlds). Planets in the mass range of 10–15  $M_{\oplus}$ , if half-ice and half-rock by mass, have radii of 2.5  $R_{\oplus}$ , which exactly match the second peak of the exoplanet radius bimodal distribution. Any planet in the 2- to 4- $R_{\oplus}$  range requires a gas envelope of at most a few mass percentage points, regardless of the core composition. To resolve the ambiguity of internal compositions, we use a growth model and conduct Monte Carlo simulations to demonstrate that many intermediate-size planets are “water worlds.”

exoplanets | bimodal distribution | ices | water worlds | planet formation

Thousands of exoplanets discovered during the last two decades cover a wide range of masses and sizes. In the 1- to 20- $M_{\oplus}$  and 1- to 4- $R_{\oplus}$  ranges, several types of planets have been identified. The planets with high densities are considered rocky, while the ones with low densities have been modeled either as gas dwarfs or water worlds. The gas dwarfs are thought to have a rocky core enveloped in a  $H_2$ –He gaseous envelope, while the water worlds contain a significant amount of multicomponent,  $H_2O$ -dominated ices/fluids in addition to rock and gas.

Here, we focus on such small planets, namely, the super-Earths (1–2  $R_{\oplus}$ ) and the sub-Neptunes (2–4  $R_{\oplus}$ ). Mass–radius curves (Figs. 1 and 2) show that they contain a few percent of gas by mass at most; that is, their masses are dominated by the cores that must have formed by the accretion of solids in the disk.

The measurements of planetary radii and orbital periods of more than 4,000 confirmed or candidate exoplanets by the National Aeronautics and Space Administration *Kepler* mission (1–6) revealed a bimodal distribution of planet sizes in the 1- to 4- $R_{\oplus}$  range. This discovery was interpreted as the evidence for the presence of two populations of planets—smaller rocky worlds and the intermediate-size planets, which, because of their proximity to the host star, were interpreted as gas dwarfs rather than water worlds.

Further refinement of the host stellar parameters by the *Gaia* astrometry mission (7–11) yields a better resolved bimodal distribution of planetary radii with two peaks and a local minimum or gap at 1.8–2  $R_{\oplus}$  (Figs. 1 and 2). The gap separates two subpopulations of planets on the mass–radius diagram (Figs. 1 and 2): super-Earths (1–2  $R_{\oplus}$ ) and sub-Neptunes (2–4  $R_{\oplus}$ ). Whether this gap is a direct result of planet formation or a secondary feature formed by photoevaporation of gas envelopes is debated. The distances to the host stars in both subpopulations appear to

be distributed log-uniform, that is, flat in semimajor axis  $a$  or orbital period  $P$ , beyond  $\sim 10$  d (figure 7 of ref. 12). Such orbit distributions of both populations challenge the photoevaporation scenario as the cause of the gap because it strongly depends on the orbital distance. If the gap is caused by photoevaporation, then an anticorrelation in their orbital distributions is expected (13). We interpret the flatness in distributions as additional evidence for both populations arising from their intrinsic properties (14).

The distinction between gas dwarfs and water worlds cannot be made based on the mass–radius relationship alone or the presence or lack of a  $H_2$ –He gas layer (15). Therefore, we invoke a mass–radius distribution among small planets and their growth models to argue that at least some intermediate-size planets are water worlds.

Protoplanetary disks of solar-like composition contain three principal planet-building components—nebular gas,  $H_2O$ -rich ices, and rocky [silicates-plus-(Fe,Ni)-metal] materials—whose compositions are a function of element volatility (characterized by the equilibrium condensation temperatures; Fig. 3) and, therefore, change radially and temporally with changing temperature. In the case of cooling, a gradual decrease in temperature results in progressive condensation of Fe–Mg–Ca–Al silicates and (Fe,Ni)-metal making up 0.5% of the total disk mass at  $\sim 1,000$  K, until C,N,O,H-bearing ices (1.0% total mass) start to sequentially condense below  $\sim 200$  K. The condensation of ices is a sharp feature in the protoplanetary disk. Once the temperature drops a bit (a few kelvins) below its condensation temperature, a very large amount of ice would form. In the case of heating, for example, due to inward dust drift, the sequence of phase changes reverses. The disk never gets cold enough for

## Significance

The discovery of numerous exoplanet systems containing diverse populations of planets orbiting very close to their host stars challenges the planet formation theories based on the solar system. Here, we focus on the planets with radii of 2–4  $R_{\oplus}$ , whose compositions are debated. They are thought to be either gas dwarfs consisting of rocky cores embedded in  $H_2$ -rich gas envelopes or water worlds containing significant amounts of  $H_2O$ -dominated fluid/ice in addition to rock and gas. We argue that these planets are water worlds.

Author contributions: L.Z., S.B.J., D.D.S., M.I.P., and A.V. designed research; L.Z., S.B.J., D.D.S., M.I.P., A.V., J.P.-M., T.R.M., G.L., H.C., A.L., and M.Z.H. performed research; L.Z., S.B.J., D.D.S., M.I.P., A.V., M.L.-M., J.P.-M., T.R.M., G.L., M.Z.H., A.S.B., M.D., T.A.B., H.C., and R.D.W. analyzed data; and L.Z., S.B.J., D.D.S., M.I.P., A.V., M.L.-M., T.R.M., G.L., M.Z.H., H.C., and A.L. wrote the paper.

The authors declare no conflict of interest.

This article is a PNAS Direct Submission.

Published under the PNAS license.

<sup>1</sup>To whom correspondence should be addressed. Email: astrozeng@gmail.com.

This article contains supporting information online at [www.pnas.org/lookup/suppl/doi:10.1073/pnas.1812905116/-DCSupplemental](http://www.pnas.org/lookup/suppl/doi:10.1073/pnas.1812905116/-DCSupplemental).





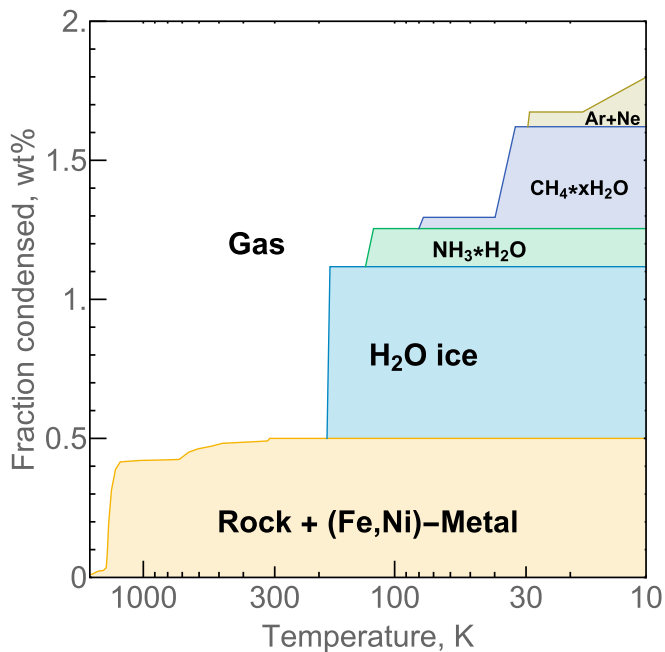


**Fig. 3.** The stability fields of planet-building materials in a protoplanetary disk of solar composition at  $10^{-4}$  bar. The fraction of condensed rocky matter ( $>200$  K) is calculated with the GRAINS code (58), while condensation temperatures and abundances of ices are taken from ref. 59. The composition of gas is temperature dependent and always complementary to the composition of the condensed phase assemblage.

To interpret the observed mass–radius distributions, we modeled the growth curves of planets by adding either ice or gas to a rocky core (*Materials and Methods* and *SI Appendix*).

The mass distributions of small planets are compared with each other (Fig. 2, histograms on the  $x$  axis) and the calculated growth tracks (Fig. 1). Planets of  $1.4\text{--}1.9 R_{\oplus}$  and  $2\text{--}3 R_{\oplus}$  are compared, where each bin contains about 20 planets (*SI Appendix, Table S1*). The mass distributions of sub-Neptunes range from 3 to  $20 M_{\oplus}$ , while super-Earths truncate at  $10 M_{\oplus}$ . The first population has masses of  $5.3 \pm 1.5 M_{\oplus}$ . The second population has masses of  $8.3 \pm 3 M_{\oplus}$ . The offset of  $3 M_{\oplus}$  suggests that the cores of the second population are significantly more massive, which coincides with adding ice to rock (Fig. 1, cyan arrows, growth curves of ices).

Bimodal mass distribution of the radial-velocity (RV) sub-Neptune population ( $2\text{--}4 R_{\oplus}$ ) is identified, and the higher peak of this, with the mass of  $\sim 16 M_{\oplus}$ , may result from the merging of primary icy cores. This can explain why Uranus (33), Neptune, and similar planets did not accrete significant amount of  $\text{H}_2$ -plus-He gas, although their final mass appears to be greater than the critical core mass (34) for a runaway gas accretion. This means that the Uranus, Neptune, and many other icy cores like them are mergers of many smaller, less massive, primordial icy cores. Each primordial core is less massive than the critical core mass. The collision and merging of two primordial cores can partially remove their  $\text{H}_2/\text{He}$  envelopes (35), if such existed, while retaining most of their core masses. The colliding icy cores are more likely to stick and merge, yielding a core of doubled mass. In contrast, a collision of two rocky cores, each bigger than  $\sim 10 M_{\oplus}$ , tends to catastrophically disrupt them rather than to merge (36).

Transit-timing-variation (TTV) planets (Fig. 2, triangles) of  $2\text{--}4 R_{\oplus}$ , on the other hand, show systematically smaller masses. They are preferably found around metal-poor host stars ( $[\text{Fe}/\text{H}]$  less than  $-0.3$ ) (37), as opposed to RV sub-Neptunes, which are found across a wide range of metallicity (12), suggesting somewhat different formation environments.

Atmospheric escape has a correlation between the escape velocities and atmospheric compositions of objects in our solar system (Fig. 4). Applying the same physics to exoplanets, one can calculate, for a given surface temperature, what gaseous species a planetary atmosphere can hold. Super-Earths and sub-Neptunes have escape velocities on the order of  $\sim 20$  km/s, marked by the contour of  $M_p/R_p = 3$  in the Earth units (Figs. 1 and 2). A value of 20 km/s roughly corresponds to the thermal escape threshold of atomic hydrogen at 150 K, or molecular hydrogen ( $\text{H}_2$ ) at 300 K, or helium at 600 K. Therefore, bodies with  $M_p/R_p < 3$  are susceptible to the escape of  $\text{H}_2$  and He. The  $\text{H}_2$  in their atmospheres/envelopes cannot last over billion-year timescale unless being continuously replenished by an underlying reservoir. It is possible that methane  $\text{CH}_4$ , ammonia  $\text{NH}_3$  (38–40), and even  $\text{H}_2$  (41) outgas gradually from an initial  $\text{H}_2\text{O}$  reservoir to replenish a primary envelope, or to form a secondary one. During this process, He and heavier species are preferentially retained (42). There is a huge density contrast among planets residing around the He escape threshold (gray dashed line labeled “Helium” in Fig. 4). Some of such planets, for example, WASP-107 b (43, 44), WASP-69 b (45), HD 189733 b (46), and HAT-P-11 b (47, 48), are observed to be surrounded by He-rich extended atmospheres suggestive of He escape from them. Because of similar temperatures and escape velocities (depth of surface gravity potential well), all planets residing there would be losing He (and  $\text{H}_2$ ) at this moment, if they have any. We infer that the He escape threshold is the boundary separating the populations of puffy hot-Saturns and small ( $<4 R_{\oplus}$ ) exoplanets. The latter likely possess higher mean molecular weight atmospheres with  $\text{H}_2\text{O}$  in their deeper interior (above a few gigapascals) partitioned among condensed phases including fluids, insulating solids, and superionic ices (49).

Water worlds have other observational evidence including the following: (i) spectroscopy of metal-polluted white dwarfs showing that some planetary debris accreted by white dwarfs are ice-rich (50, 51); (ii) transmission spectroscopy of an inflated Saturn-mass exoplanet WASP-39b that shows strong water absorption features corresponding to the estimated  $\text{H}_2\text{O}/\text{H}$  ratio of  $151\times$ solar in the planet’s atmosphere (52).

Monte Carlo simulation was used to show that the bimodal radius distribution (yellow histograms on the  $y$  axis in Figs. 1 and 2) could arise from the dichotomy of rocky and icy cores. It is performed with the following assumptions. The protoplanetary disk is assumed to have solar-like major element ratios (Fe:Mg:Si:O:C:N), inferred from the tight distribution of C/O and Mg/Si ratios around solar values in the main-sequence stars in the solar neighborhood (53). Besides the  $\text{H}_2$ -He gas, the disk contains roughly one part of Mg–silicate–rock-plus-(Fe,Ni)-metal, one part of  $\text{H}_2\text{O}$  ice, and one part of other ices (methane clathrates and ammonia hydrates, which are still dominated by the  $\text{H}_2\text{O}$  in their compositions) by mass. Due to the disk temperature gradient and condensation temperature gap between the rock-plus-metal and ice, the disk is thermally zoned into an inner zone with solid rock-plus-metal dominating, and an outer zone with both rock-plus-metal and ices (mostly  $\text{H}_2\text{O}$ ) suspended in  $\text{H}_2$ -plus-He gas.

The simulation reproduces the bimodal radius distribution (Fig. 2, blue vertical histogram). It also reproduces the mass–radius distribution of RV planets with their gap, groupings (Fig. 2, gray contours in the background), and mass offset. Planets  $>3 R_{\oplus}$  generally require the presence of a gaseous envelope.

## Conclusions

We divide exoplanets around sun-like stars into four main categories according to the cumulative planet radius distribution (14) and mass–radius diagram (Figs. 1 and 2):

- i) Rocky worlds ( $<2 R_{\oplus}$ ) consist primarily of Mg–silicate–rock and (Fe,Ni)-metal; they broadly follow the extrapolation of mass–radius relation of Earth and Venus.



$f = 1$ ; if  $x = 1$  (100% ice),  $f = 1.41$ . Interpolation gives  $f = (1 + 0.55x - 0.14x^2)$  (57). From disk element abundance, “ $x$ ” of icy cores typically range from 1/2 to 2/3, depending on the incorporation of more volatile clathrate and hydrate ices. Then, “ $x$ ” is assumed to follow a uniform distribution in-between 1/2 (solar rock/H<sub>2</sub>O-ice ratio) and 2/3 (solar rock/total-ices ratio) for icy cores. The masses of rocky and icy cores are assumed to follow their observed mass distributions, respectively (histograms on the  $x$  axis in Fig. 2). Considering the mass balance between the rock-plus-metal and ices, the number ratio of rocky to icy cores is  $\sim 1:2$ , matching the occurrence rate of super-Earths ( $1-2 R_{\oplus}$ ) versus sub-Neptunes ( $2-4 R_{\oplus}$ ) (12). With geometric transit probability, their observed number by *Kepler* is about equal. Additional  $\pm 7\%$   $1-\sigma$  Gaussian errors in  $R_p$  and  $\pm 30\%$   $1-\sigma$  Gaussian errors in  $M_p$  are included in the simulation to account for the observational uncertainties. See more details in *SI Appendix*.

- Akeson RL, et al. (2013) The NASA exoplanet archive: Data and tools for exoplanet research. *Publ Astron Soc Pac* 125:989.
- Thompson SE, et al. (2018) Planetary candidates observed by *Kepler*. VIII. A fully automated catalog with measured completeness and reliability based on data release 25. *Astrophys J Suppl Ser* 235:38.
- Zeng L, et al. (2017) Planet size distribution from the *Kepler* mission and its implications for planet formation. *48th Lunar and Planetary Science Conference* (Lunar and Planetary Institute, Houston). Available at [adsabs.harvard.edu/abs/2017LPL....48.1576Z](https://adsabs.harvard.edu/abs/2017LPL....48.1576Z). Accessed March 1, 2019.
- Fulton BJ, et al. (2017) The California-*Kepler* survey. III. A gap in the radius distribution of small planets. *Astron J* 154:109.
- Van Eylen V, et al. (2017) An asteroseismic view of the radius valley: Stripped cores, not born rocky. *Mon Not R Astron Soc* 479:4786–4795.
- Mayo AW, et al. (2018) 275 candidates and 149 validated planets orbiting bright stars in K2 campaigns 0–10. *Astron J* 155:136.
- Berger TA, Huber D, Gaidos E, van Saders JL (2018) Revised radii of *Kepler* stars and planets using *Gaia* Data Release 2. *Astrophys J* 866:99.
- Fulton BJ, Petigura EA (2018) The California-*Kepler* survey. VII. Precise planet radii leveraging *Gaia* DR2 reveal the stellar mass dependence of the planet radius gap. *Astron J* 156:264.
- G. *Gaia* Collaboration; et al. (2018) *Gaia* data release 2. Summary of the contents and survey properties. *Astron Astrophys* 616:A1.
- Lindgren L, et al. (2018) *Gaia* data release 2: The astrometric solution. *Astron Astrophys* 616:A2.
- Stassun KG, Corsaro E, Pepper JA, Gaudi BS (2017) Empirical accurate masses and radii of single stars with *TESS* and *Gaia*. *Astron J* 155:22.
- Petigura EA, et al. (2018) The California-*Kepler* survey. IV. Metal-rich stars host a greater diversity of planets. *Astron J* 155:89.
- Owen JE, Wu Y (2017) The evaporation valley in the *Kepler* planets. *Astrophys J* 847:29.
- Zeng L, Jacobsen SB, Sasselov DD, Vanderburg A (2018) Survival function analysis of planet size distribution with *Gaia* DR2 updates. *Mon Not R Astron Soc* 479:5567–5576.
- Adams ER, Seager S, Elkins-Tanton L (2008) Ocean planet or thick atmosphere: On the mass-radius relationship for solid exoplanets with massive atmospheres. *Astrophys J* 673:1160–1164.
- Öberg KI, Murray-Clay R, Bergin EA (2011) The effects of snowlines on C/O in planetary atmospheres. *Astrophys J* 743:L16.
- Hayashi C (1981) Structure of the solar nebula, growth and decay of magnetic fields and effects of magnetic and turbulent viscosities on the nebula. *Prog Theor Phys Suppl* 70:35–53.
- Stevenson DJ, Lunine JI (1988) Rapid formation of Jupiter by diffusive redistribution of water vapor in the solar nebula. *Icarus* 75:146–155.
- Desch SJ (2007) Mass distribution and planet formation in the solar nebula. *Astrophys J* 671:878–893.
- Zhang K, Pontoppidan KM, Salyk C, Blake GA (2013) Evidence for a snow line beyond the transitional radius in the TW Hya protoplanetary disk. *Astrophys J* 766:82.
- Zhang K, Blake GA, Bergin EA (2015) Evidence of fast pebble growth near condensation fronts in the HL Tau protoplanetary disk. *Astrophys J* 806:L7.
- Cieza LA, et al. (2016) Imaging the water snow-line during a protostellar outburst. *Nature* 535:258–261.
- Lee J-E, et al. (Feburary 4, 2019) The ice composition in the disk around V883 Ori revealed by its stellar outburst. *Nat Astron*, 10.1038/s41550-018-0680-0.
- Morbidelli A (2018) Accretion processes. [arXiv:1803.06708](https://arxiv.org/abs/1803.06708).
- Morbidelli A, Lambrechts M, Jacobson S, Bitsch B (2015) The great dichotomy of the solar system: Small terrestrial embryos and massive giant planet cores. *Icarus* 258: 418–429.
- Piso A-MA, Öberg KI, Birnstiel T, Murray-Clay RA (2015) C/O and snowline locations in protoplanetary disks: The effect of radial drift and viscous gas accretion. *Astrophys J* 815:109.
- Sasselov DD, Lecar M (2000) On the snow line in dusty protoplanetary disks. *Astrophys J* 528:995–998.
- Sato T, Okuzumi S, Ida S (2016) On the water delivery to terrestrial embryos by ice pebble accretion. *Astron Astrophys* 589:A15.
- Martin RG, Livio M (2012) On the evolution of the snow line in protoplanetary discs. *Mon Not R Astron Soc Lett* 425:L6–L9.
- Kley W, Nelson RP (2012) Planet-disk interaction and orbital evolution. *Annu Rev Astron Astrophys* 50:211–249.
- Raymond SN, et al. (2009) Planet-planet scattering leads to tightly packed planetary systems. *Astrophys J* 696:L98–L101.
- Johansen A, Lambrechts M (2017) Forming planets via pebble accretion. *Annu Rev Earth Planet Sci* 45:359–387.
- Kegerreis JA, et al. (2018) Consequences of giant impacts on early Uranus for rotation, internal structure, debris, and atmospheric erosion. *Astrophys J* 861:52.
- Rafikov RR (2006) Atmospheres of protoplanetary cores: Critical mass for nucleated instability. *Astrophys J* 648:666–682.
- Inamdar NK, Schlichting HE (2015) The formation of super-Earths and mini-Neptunes with giant impacts. *Mon Not R Astron Soc* 448:1751–1760.
- Marcus RA, Stewart ST, Sasselov D, Hernquist L (2009) Collisional stripping and disruption of super-Earths. *Astrophys J* 700:L118–L122.
- Brewer JM, Wang S, Fischer DA, Foreman-Mackey D (2018) Compact multi-planet systems are more common around metal-poor hosts. *Astrophys J* 867:L3.
- Levi A, Sasselov D, Podolak M (2013) Volatile transport inside super-Earths by entrapment in the water-ice matrix. *Astrophys J* 769:29.
- Levi A, Sasselov D, Podolak M (2014) Structure and dynamics of cold water super-Earths: The case of occluded CH<sub>4</sub> and its outgassing. *Astrophys J* 792:125.
- Levi A, Kenyon SJ, Podolak M, Pralnick D (2017) H-atmospheres of icy super-Earths formed in situ in the outer solar system: An application to a possible Planet Nine. *Astrophys J* 839:111.
- Soubiran F, Millitzer B (2015) Miscibility calculations for water and hydrogen in giant planets. *Astrophys J* 806:228.
- Hu R, Seager S, Yung YL (2015) Helium atmospheres on warm Neptune- and sub-Neptune-sized exoplanets and applications to GJ 436b. *Astrophys J* 807:8.
- Anderson DR, et al. (2017) The discoveries of WASP-91b, WASP-105b and WASP-107b: Two warm Jupiters and a planet in the transition region between ice giants and gas giants. *Astron Astrophys* 604:A110.
- Spake JJ, et al. (2018) Helium in the eroding atmosphere of an exoplanet. *Nature* 557: 68–70.
- Nortmann L, et al. (2018) Ground-based detection of an extended helium atmosphere in the saturn-mass exoplanet WASP-69b. *Science* 362:1388–1391.
- Salz M, et al. (2018) Detection of He I  $\lambda 10830$  Å absorption on HD 189733 b with CARMENES high-resolution transmission spectroscopy. *Astron Astrophys* 620:A97.
- Allart R, et al. (2018) Spectrally resolved helium absorption from the extended atmosphere of a warm Neptune-mass exoplanet. *Science* 362:1384–1387.
- Mansfield M, et al. (2018) Detection of helium in the atmosphere of the exo-Neptune HAT-P. *Astrophys J* 868:L34.
- Millot M, et al. (2018) Experimental evidence for superionic water ice using shock compression. *Nat Phys* 14:297–302.
- Farihi J, Gänsicke BT, Koester D (2013) Evidence for water in the rocky debris of a disrupted extrasolar minor planet. *Science* 342:218–220.
- Raddi R, et al. (2015) Likely detection of water-rich asteroid debris in a metal-polluted white dwarf. *Mon Not R Astron Soc* 450:2083–2093.
- Wakeford HR, et al. (2017) The complete transmission spectrum of WASP-39b with a precise water constraint. *Astron J* 155:29.
- Brewer JM, Fischer DA (2016) C/O and Mg/Si ratios of stars in the solar neighborhood. *Astrophys J* 831:20.
- Bhattacharya A, et al. (2018) WFIRST exoplanet mass measurement method finds a planetary mass of  $39 \pm 8 M_{\oplus}$  for OGLE-2012-BLG-0950Lb. *Astron J* 156:289.
- Suzuki D, et al. (2016) The exoplanet mass-ratio function from the MOA-II survey: Discovery of a break and likely peak at a Neptune mass. *Astrophys J* 833:145.
- Zeng L, Sasselov DD, Jacobsen SB (2016) Mass-radius relation for rocky planets based on PREM. *Astrophys J* 819:127.
- Zeng L, Sasselov D (2013) A detailed model grid for solid planets from 0.1 through 100 Earth masses. *Publ Astron Soc Pac* 125:227–239.
- Petaev MI (2009) The GRAINS thermodynamic and kinetic code for modeling nebular condensation. *Calphad* 33:317–327.
- Lewis JS (1972) Low temperature condensation from the solar nebula. *Icarus* 16: 241–252.
- Chamberlain JW, Hunten DM (1987) *Theory of Planetary Atmospheres: An Introduction to Their Physics and Chemistry* (Academic, New York).